Evaluation of a mine panel failure using the local mine stiffness criterion — a case study

K. Morsy and S.S. Peng
Graduate research assistant and chairman, respectively, Mining Engineering Department,
West Virginia University, Morgantown, West Virginia

Abstract

A new method of pillar stability evaluation was proposed. The unique feature about the method is that it estimates two types of stability factors for the pillar. The first stability factor is to measure how much the applied stress at that point is smaller than its strength, and the second stability factor is to predict whether or not the pillar will fail violently. The strain-softening behavior of coal pillars was simulated by the Drucker-Prager yield criterion. A new algorithm that simulates the strain-hardening behavior of the gob was used. A numerical technique to estimate the local mine stiffness (LMS) was introduced and verified by both numerical and analytical methods. A case of massive pillar failure in a room-and-pillar mine was used to define the stability limits for the proposed method.

Introduction

It is well known that stress distributions in coal pillars are not only nonuniformly distributed but are also dependent on their location in the panel or section of a coal mine. The former is due to the friction effect at the boundaries between the roof/floor and coal pillar, whereas the latter was due to the distance from the abutment pillars (or panel/section edges) and/or pillar line or longwall retreating face. It follows that pillar failure is progressive, i.e., it starts in the areas with the highest stresses and propagates towards the elastic areas in accordance with the selected failure criteria. Therefore, it is certain that some areas in the pillar are subjected to a stress levels less than their strengths while, at same time, other areas are experiencing stresses in the post-failure region. Consequently, to fully account for the progressive failure of a coal pillar, the constitutive relation employed must cover the complete stress-strain curve of the coal. However, it is well known that the pillar stability in its post-peak region depends on the stiffness of the mine roof/floor structure, as compared to that of coal on the post-peak region.

Although the local mine stiffness (LMS) criterion has been established for a long time to predict the pillars stability in the post-peak region (Starfield and Fairhurst, 1968; Salamon, 1970), there are only limited applications of LMS criterion for practical mining problems, such as pillar design (Pen and Barron, 1994; Sheorey et al., 1995; Zipf, 1999). The authors believe that, until now, there is no available pillar design methodology that implements the LMS criterion.

This paper illustrates the development of a pillar design method for evaluating the pillar stability using LMS criterion. A case study is used to validate the proposed method.

Proposed pillar design procedure

Both the laboratory (Das, 1986) and in situ tests (Wagner, 1974; Van Heerden, 1975) on coal pillars show a marked degree of strain softening. The nonlinear behavior has usually been simulated by gradually altering the elastic modulus of yielding material using a quasi-elastic approach (Chen and Karmis, 1988). In this paper, the extended Drucker-Prager yield criterion with strain softening was used for the simulation of the yielding mechanism of coal pillar.

The procedure for the proposed coal-pillar design method involves two steps:

- First, the state of stress throughout the whole pillar is determined. In addition, the LMS distribution at the examined pillar is determined. Therefore, two types of local stability factors can be calculated. Type I local stability factor (LSF1) is for those points at which the state of stress is located in the region OB (Fig. 1), and Type II local stability factor (LSF2) is for those points where the state of stress is in the region BC (Fig. 1).
- Second, the global pillar stability factors SF1 and SF2 are determined by averaging the corresonding local stability factors

The unique feature about this method is that it recognizes that the pillar stresses and the LMS are not uniformly distributed.

For those points where the state of stress is located in the OB region, the stability factor (or the local stability factor LSF1) for an individual point is determined by comparing its state of stress to the failure stress defined by the Drucker-Prager yield criterion (Hibbitt et al., 1998) according to

Preprint number 01-183, presented at the SME Annual Meeting, Feb. 26-28, 2001, Denver, Colorado. Original manuscript was accepted for publication November 2001. However, author submitted a revised text December 2002. Discussion of this peer-reviewed and approved paper is invited and must be submitted to SME Publications Dept. prior to Sept. 30, 2003.

$$LSF1 = \frac{d + P\tan\beta}{Q} \qquad (1)$$

where

$$P = \frac{1}{3}(\sigma_1 + \sigma_2 + \sigma_3) \ ;$$

$$Q = \sqrt{\frac{1}{2}(\sigma_1 \pm \sigma_2)^2 + (\sigma_1 - \sigma_3)^2 + (\sigma_2 - \sigma_3)^2} \ ;$$

d and β are material properties; and
σ_1, σ_2 and σ_3 are the principal stresses.

Because it is not possible to have LSFI < 1, the possible values for LSF1 at any point within the pillar are either 1 or >1.

Once the state of stress for an individual point has passed the peak strength, it is in the yielding region BC (Fig. 1) in which two types of yielding conditions can be expected:

- *stable yielding*, in which the roof load at any instant is less than the residual pillar strength at that instant, and
- *unstable yielding*, which occurs when the rock mass applies a load greater than that of the pillar's residual strength.

To assess the local stability factors for those points whose state of stress is located in this region, the Type II local stability factor, LSF2, is proposed as

$$LSF2 = 1 \ \text{if} \ \frac{|K_{LMS}|}{|K_p|} > 1 \ , \quad \text{for stable yielding} \qquad (2)$$

$$LSF2 = 0 \ \text{if} \ \frac{|K_{LMS}|}{|K_p|} \le 1 \ , \quad \text{for unstable yielding} \qquad (3)$$

where

$|K_{LMS}|$ is the absolute value of the local mine stiffness at the point of interest and

$|K_p|$ is the absolute value of the minimum post-peak slope of the stress-strain curve at the point of interest.

Table 1 summarizes the three possible combinations of local stability factors at any point within the pillar.

To assess the overall pillar stability, the global stability factors SF1 and SF2 are used. The global stability factors are obtained separately by averaging the corresponding type of the local stability factor, LSF1 or LSF2. Back analysis for different cases of pillar failure is the most suitable approach to determine the possible combinations of SF1 and SF2 for stable and unstable pillar conditions.

New approach to estimate the local mine stiffness

Starfield and Wawersik (1968) introduced the local mine stiffness concept to explain the violent failure of pillars. The LMS concept can be explained by considering a hypothetical situation (Fig. 2 A) in which a pillar is replaced by a hydraulic jack. Initially, this jack is pressurized high enough to prevent roof convergence. As the jack is slowly released, the force imposed on it will drop because more loads are transferred to the adjacent pillars. As the jack force is released, roof sagging and floor heaving occur at the jack location. While the roof

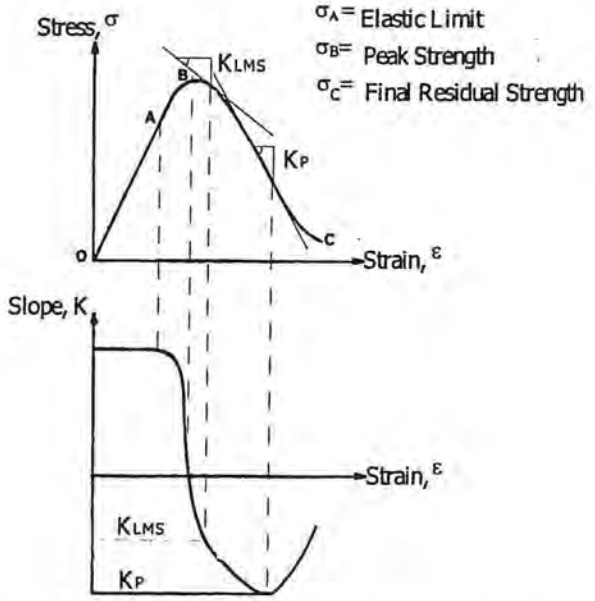

Figure 1 — Complete stress-strain curve for coal.

Table 1 — Possible combinations of LSFs at each individual point within the pillar.

Combination	LSFI	LSF2
I	>1	1
II	1	1
III	1	0

remains intact, a linear relation between the jack force and the roof-to-floor convergence could be assumed (Fig. 2 B). The slope of this line is called the local mine stiffness, K_{LMS}.

There are two approaches for estimating the K_{LMS} at a pillar site: the analytical approach developed by Salamon (1970) and the numerical approach proposed (perturbation method) by Starfield and Wawersik (1968). These approaches consider the pillar and surrounding strata to be homogeneous, isotropic and linear elastic. In addition, it is assumed that the stress within the pillar is uniformly distributed.

In this paper, to estimate the K_{LMS} at a specific pillar site, the effect of the hypothetical experiment proposed by Starfield and Fairhurst (1968) (Fig. 2A) is numerically simulated using the finite element approach. It is assumed that a pillar could be replaced by a series of hydraulic jacks. The number of jacks should be large enough so that the load and roof-to-floor convergence could be assumed uniform at each jack. These jacks exert different forces to the roof and floor depending on their locations within the pillar. By removing the pillar (releasing the jacks), the finite element program ABAQUS (Hibbitt et al., 1998) first applies the forces that the pillar is exerting on the roof and floor at the nodes of interface. These forces are then ramped down gradually to zero during the pillar removal process. During the pillar removal process, the vertical stresses and displacements are monitored for the immediate roof and floor at the location of the removed pillar. At each jack location, which is represented by two vertically aligned nodes, the K_{LMS} is determined by the slope of the relation between the recorded stresses and the roof-to-floor convergences divided by the seem height (Fig. 2 B).

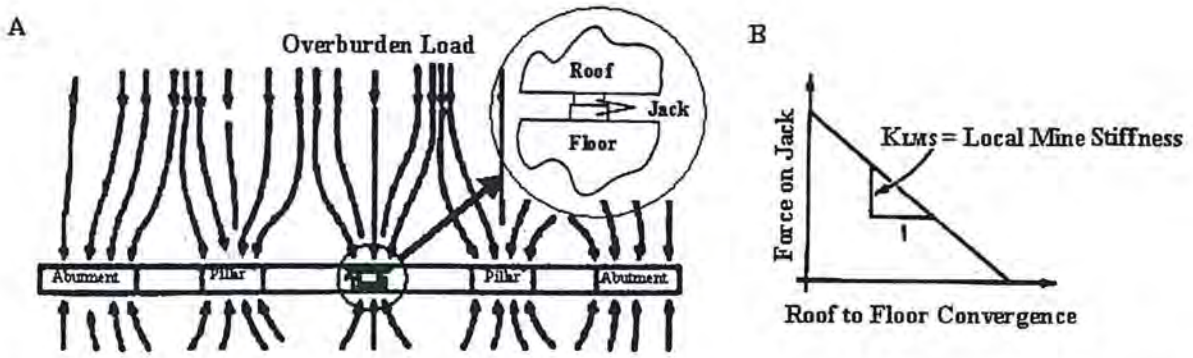

Figure 2 — Illustration of local mine stiffness concept: (A) A hydraulic jack replaces a coal pillar; (B) K_{LMS} is the slope of jack vs. the roof-to-floor convergence.

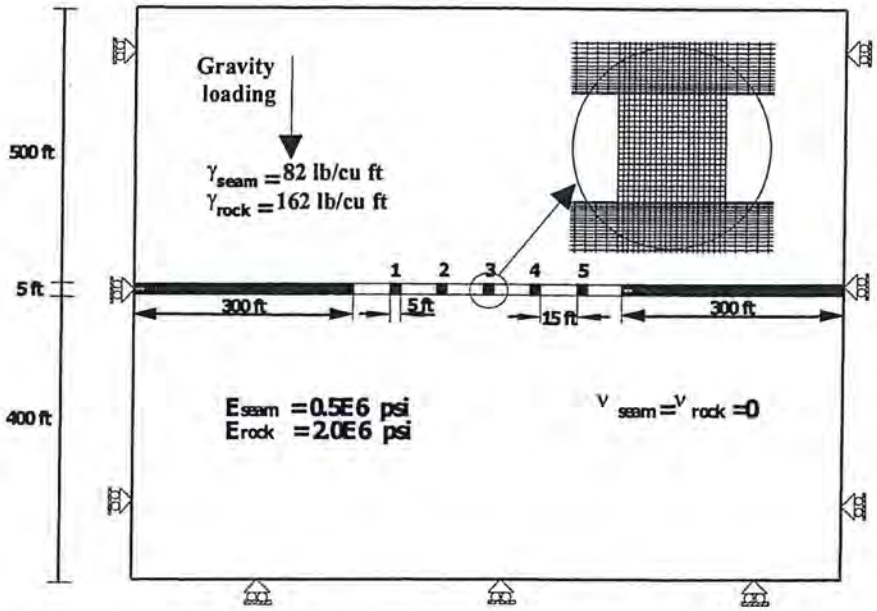

Figure 3 — Configuration of finite element model used for estimating K_{LMS}.

The numerical method used to evaluate the K_{LMS} was tested against the analytical solution of a simple case provided by Salamon (1970). This example assumes a panel of five long pillars in elastic homogeneous isotropic infinite medium. The pillar height and width are 1.5 m (5 ft) and the entry width is 4.5 m (15 ft). The overall dimension of this problem is shown in Fig. 3. A two-dimensional isoperimetric quadrilateral plane strain finite element model was used to simulate this panel. A large number of elements and nodes (96,800 and 97,461, respectively) were used in this model. The smallest element size in the areas of interest is 76.2 x 33.5 mm (0.25 x 0.11 ft). The boundary conditions and the material properties used in this model are presented in Fig. 3.

Because of model symmetry, the K_{LMS} was calculated only for Pillars No. 1, 2 and 3 (Fig. 3) by repeatedly applying the proposed procedure. Figure 4 shows the reduced values of the recorded stresses and strains at the center locations of Pillars No. 1, 2 and 3 while removing these pillars. The slope of the stress-strain relationship for each pillar location represents the K_{LMS} at this location. Figure 5 shows the distribution of K_{LMS} across the pillar width, it is obvious that the K_{LMS} is not uniformly distributed across the pillar. This behavior is due to the nonuniform distribution of vertical stress and roof-to-floor convergence across the pillar width. Data analysis shows that in Pillar No. 3, in spite of the fact that a majority of the area in the pillar has a uniform stress concentration (≈3), there are small zones of nonuniform stress concentration. Salamon (1970) estimated an error of 8% in K_{LMS}, determined by his analytical approach due to the nonuniform stress distribution within the pillar.

Figure 6 shows the average values of K_{LMS} for Pillars No. 1, 2 and 3 locations, estimated by the proposed approach as compared with both the analytical and perturbation approaches. Generally, the estimated values of K_{LMS} using the proposed approach are smaller than those of the corresponding analytical methods, which means that the propsoed approach is more conservative. The difference percentages between the estimated K_{LMS} and the ones calculated by Salamon for Pillars No. 1, 2 and 3 locations are 12.29%, 9.22% and 8.66%, respectively.

Because the difference percentages are very close to that estimated by Salamon (especially at Pillar No. 3), it can be concluded that the proposed approach for estimating the K_{LMS} was able to consider the nonuniformity of stress distribution within the pillars and thus more accurate.

Case study

Mine layout and failure description. The mine employed room-and-pillar mining with pillar extraction. The mining height consisted of 3.35 m (11 ft) of coal and shale under an overburden depth of 104 m (340 ft). The 47-m- (155-ft-) thick interburden, between the lower seam (the seam of interest) and the upper seam, which was mined out three to four months earlier, consisted of thick layers of sandy shale and sandstone. The immediate floor changes continuously from thick sandy shale to thin layer of claystone (Fig. 7).

The mains were developed by a 10-entry system with 6.1-m- (20-ft-) wide entries and 12.2- x 21.3-m (40- x 70-ft) chain pillars. The room-and-pillar panels consisted of 10-entry on development with chain pillars 9.1 x 24.4 m (30 x 80 ft) and entry/crosscuts 6.1-m (20-ft) wide (Fig. 8). Retreat pillar mining was implemented using four units of mobile roof supports (MRS) with 540-t (600-st) yield load capacity.

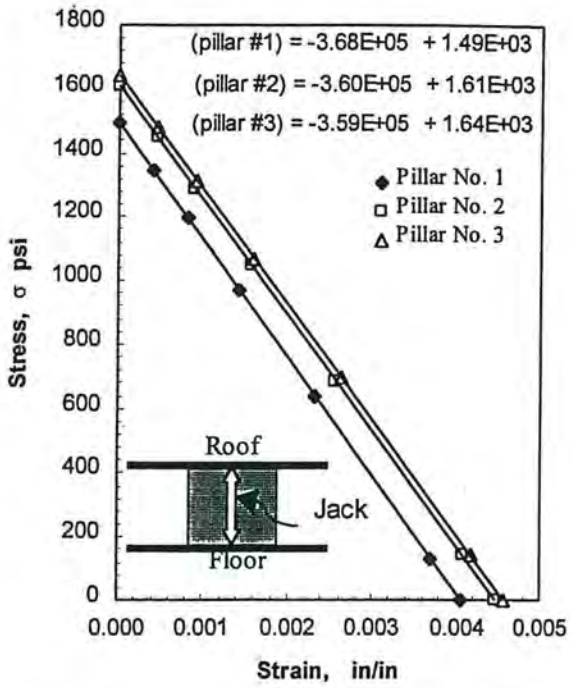

Figure 4 — Stress-strain relations at the pillar center.

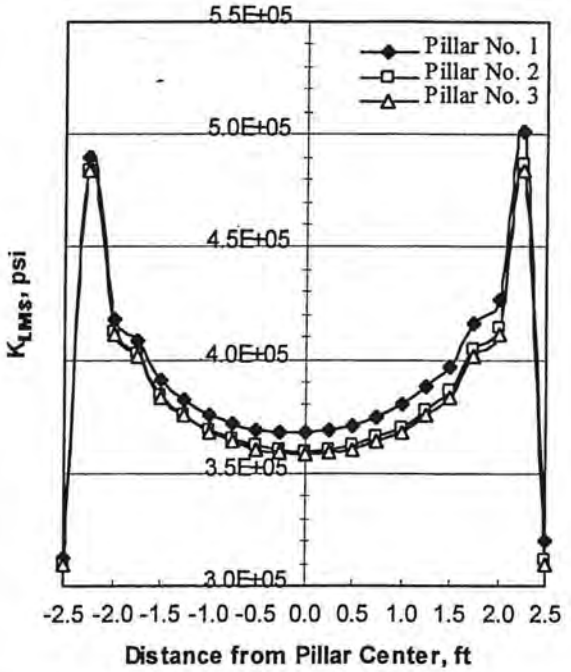

Figure 5 — Distribution of K_{LMS} across pillar width.

The term "mountain seams" refers to those seams in Central Appalachian coalfields that are associated with vertical fractures extending from the seam level all the way to the surface. These fractures are usually filled with weak clayey materials of varying thickness and are often associated with water. During development, mountain seams conditions were found in the northern part near the outcrop areas of the panel. To avoid these weak roof areas, pillar mining did not start from the limit of mining near the outcrop line. Instead, it began from the 4th and 9th row in the NE and NW sides, respectively (Fig. 8). Pillar mining for the 1st row (Pillars 1 through 12) were completed without any problem. When pillar mining for Pillar 18 in the 2nd row was proceeding, water started to flow

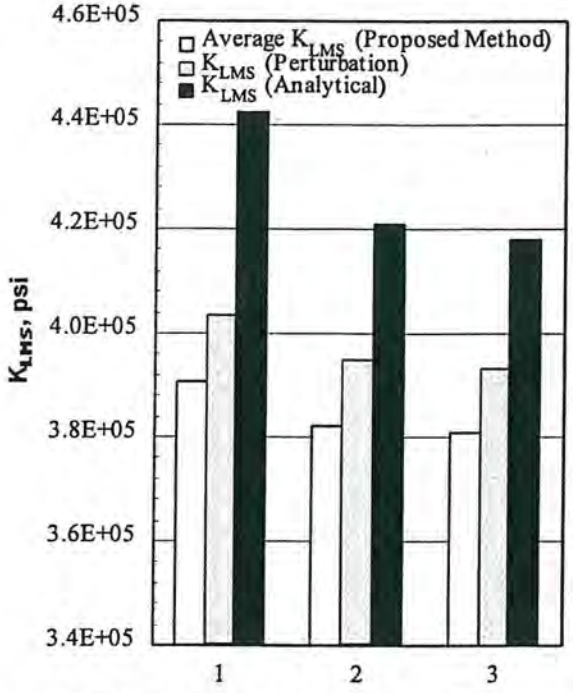

Figure 6 — Average K_{LMS} for locations at Pillars No. 1, 2 and 3.

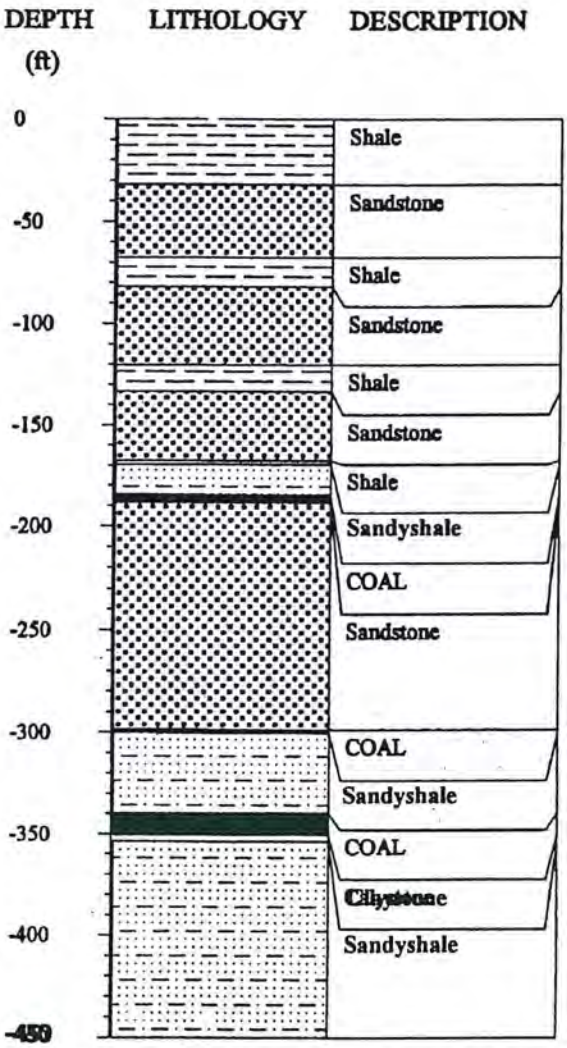

Figure 7 — Typical stratigraphic column for the study area.

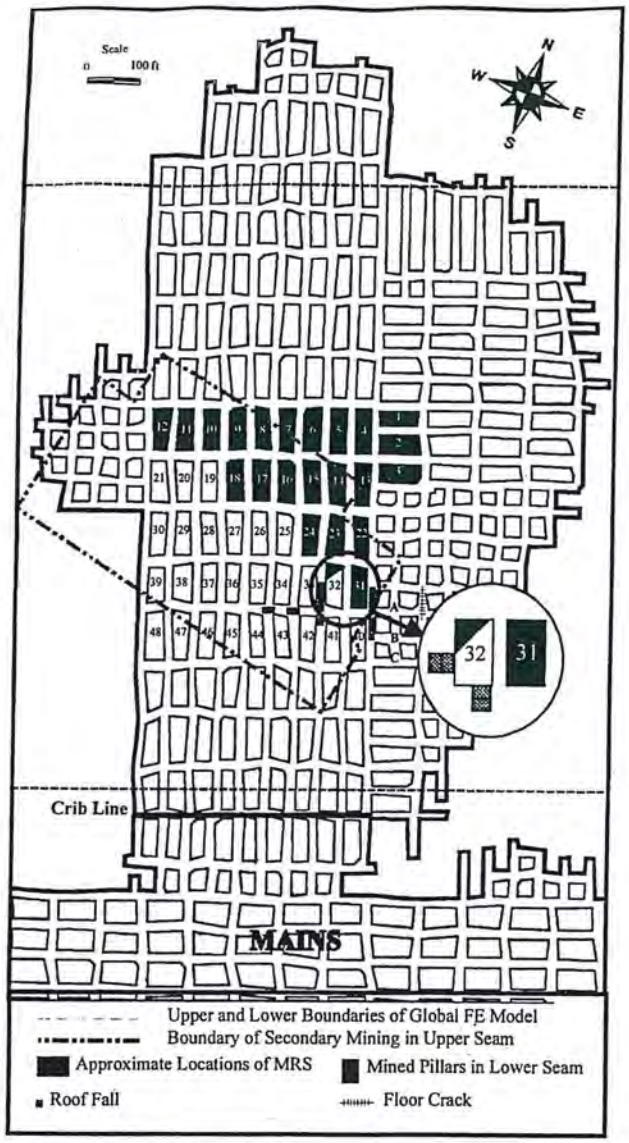

Figure 8 — Plan view of mine layout.

Figure 9 — Condition of 1st entry after failure.

Figure 10 —Typical entry conditions after failure.

from the gob between Pillars 9 and 10 to the low area in Pillars 19 through 21 and 28 through 30, where the floor soon became too muddy for mining equipment to operate. Therefore, Pillars 19 through 21 in the 2nd row were left alone. In the 3rd row, when pillar mining was completed for Pillar 24, the entry between Pillars 25 and 26 had deteriorated so badly that it was unsafe to perform any type of work there. In this entry, the ribs on both sides had spalled off more than 0.9-m (3-ft) deep, and the roof had converged considerably. Similar conditions were found in the entry between Pillars 26 and 27. Thus, Pillars 25 through 30 in the 3rd row were left alone. In the 4th row, Pillar 31 was mined successfully. However, after a few cuts in the inby side of Pillar 32, roof falls occurred at the intersections of Pillars 33 through 35 and 42 through 44 (Fig. 8). Overnight, approximately 12 hours later, the roof outby the MRS, approximately 1.2-m (4-ft) high, in the entry between Pillars 32 and 33 fell off all the way to the immediate outby intersection.

Five days after the entry roof fall, the authors performed a roof inspection. A cribline (Figs. 8 and 9) had been erected in the outby side to danger-off the section. Viewing inby from this cribline, the ribs in all entries (except the solid coal side in the 1st and 10th entries counting from left to right in Fig. 8) were spalled off badly on the top and coal fragments piled up on the floor (Fig. 10). The roof was intact or slightly peeled off. Some floor cracks and floor heave were observed in the intersections. In Crosscuts A and B (Fig. 8), roof rocks viewed from a distance had sheared off vertically from the pillar ribs and filled the whole crosscut/entry intersections. However, in Crosscut C, there were no roof fall signs. There were numerous water pools, some of which were fairly deep. The floor was muddy and deep. Inby the cribline, the floor is soft and thick while in the outby area, the soft floor layer is thin and underlain by hard rock.

The authors again toured the panel 67 days after the entry roof fall. Spalling of ribs in all entries/crosscuts had overrode the cribline and spread into the Mains. Water pooling was found everywhere, and the floor was muddy and filled with coal fragments. However, the roof remained in good condition.

Numerical modeling. The ABAQUS finite element code (Hibbitt et al., 1998) was employed to simulate the complex in situ coal pillar failure mechanisms. Three-dimensional finite element models with eight-node brick elements were used throughout all the analysis. Because the massive pillar failure problems require large three-dimensional finite element models, only one global three-dimensional model was

established (Fig. 11). The dimensions of the global model were large enough, i.e., 427 x 369 x 138 m (1,400 x 1,210 x 453 ft), to isolate the effect of boundary conditions on the area of interest. All four side boundaries and the bottom boundary of the model are roller-constrained. A large number of elements and nodes (98,298 and 114,048, respectively) were used in the global mode. The smallest element size at the area of interest is 3.0 m (10 ft). Linear elastic materials have been assigned for the global model, except for the gob material. A proposed gob model was assigned to the gob areas in the upper and lower seams (Morsy and Peng, 2001).

Due to the large dimensions of the mine panel, two-step modeling (global and submodel) was used. In both modeling steps, the model was solved in three steps to simulate three stages of mining. Stage No. 1 is the development stage of the panel, and Stages No. 2 and No. 3 are for various stages in secondary mining (Fig. 12)

In the global model, Pillars 1 through 18 (Fig. 8) were removed gradually in Stage No. 2, while Pillars 19 through 22 were removed gradually in Stage No. 3. The wet floor condition was considered in Stage No. 3 by reducing the Young's modulus of the immediate floor by 50% (Chugh and Pytel, 1992).

Using the submodeling feature in ABAQUS (Hibbitt et al., 1998), a detailed pillar stability analysis had been conducted for four locations A, B, C and D (Fig. 12). Two of them (A and B) were located below the gob of the upper seam, and the other locations (C and D) were located outside the zone of upper seam gob. The dimensions of the three submodels were identical, i.e., 45.7 x 9.1 x 26.6 m (150 x 30 x 87.33 ft), (Fig. 13). The number of elements and nodes used in submodel were 24,000 and 32,513, respectively. The pillars were modeled by small cubical elements of 1.2-m (4-ft) size. The elastic-perfectly plastic materials obeying the Drucker-Prager yield criterion were assigned to the roof and floor strata, while elastic-strain softening material obeying the Drucker-Prager yield criterion was assigned to the coal pillars. The mechanical properties used for the global model and submodels are shown in Table 2. The coal/rock interfaces were assumed to have a frictional coefficient of 0.25 (Su and Hasenfus, 1998). Basically, just like the global model, each submodel was solved in three steps except for Submodel C.

Additional steps were added to the solution to estimate the local mine stiffness at some stages of mining for the central pillars of the submodels. To simulate the wet floor conditions, the mechanical properties of the immediate floor were reduced as illustrated in Table 2. In addition, the frictional coefficient of coal/rock interface was reduced to 0.1.

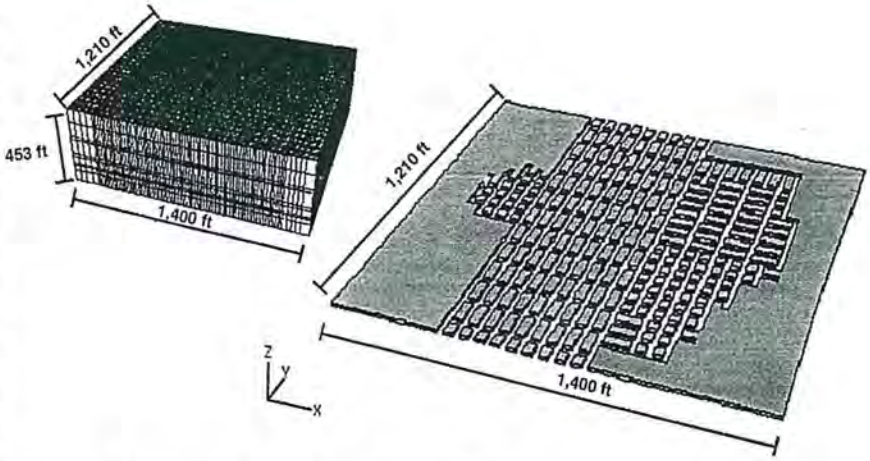

Figure 11 — Global model configurations.

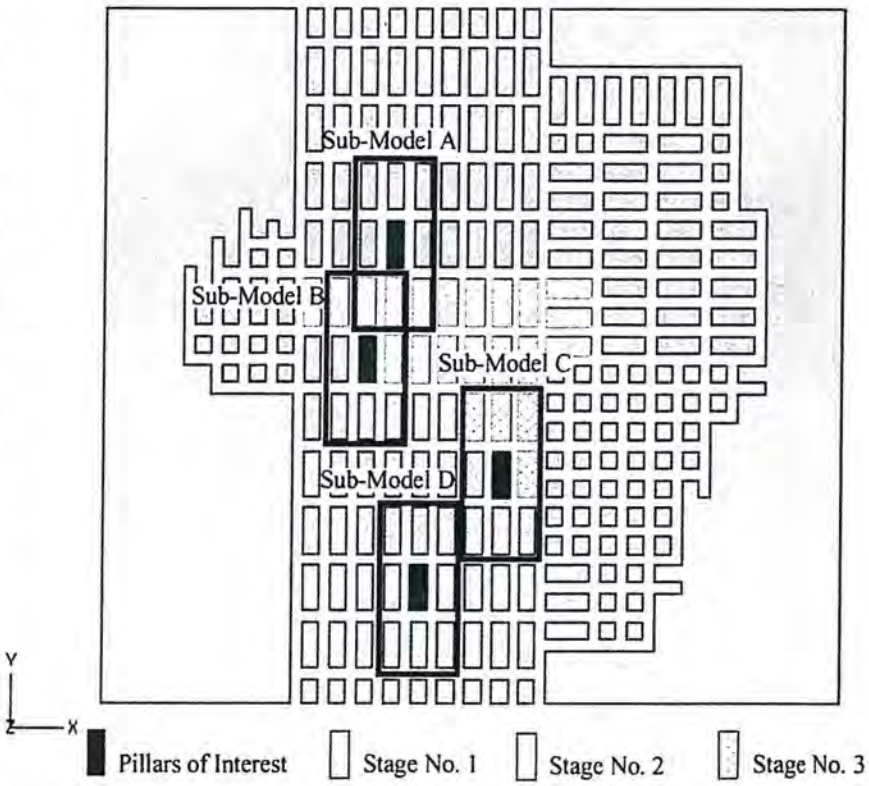

Figure 12 — Plan view for the global model at lower seam level showing the locations of submodels.

Description of the elastic-strain softening model for coal. Establishing representative coal properties for finite element analysis is the most critical step in the model formulation. The strain-softening approach has been identified as a reasonable method to describe coal behavior (Crouch and Fairhurst, 1973). Although the strain-softening concept has been used, little specific information is available concerning the construction of the strain-softening model (Karabin and Evanto, 1999). The technique used by Karabin and Evanto (1999) was used to describe the softening behavior of coal seam.

Figure 14 shows the complete stress-strain curve of coal seam used in this study. Two levels of residual strengths, R1 and R2, defined the softening part (Karabin and Evanto, 1999).

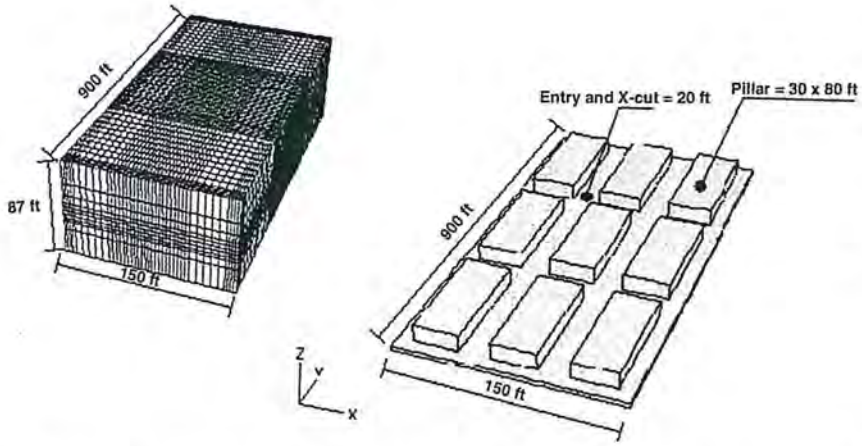

Figure 13 — Submodel configurations for Submodels A, B and C.

Table 2 — Mechanical parameters of the rocks.

Rock type	Young's modulus, psi	Poisson's ratio, ν	UCS, psi	Drucker-Prager constants β, degrees	Drucker-Prager constants d, psi
Coal	0.22	0.25	867	48.1	545
Claystone (dry)	0.152	0.27	723	49.2	135
Claystone (wet)	0.076	0.39	560	39	37
Sandshale	1.68	0.25	1,300	45.8	855
Sandstone	0.74	0.34	1,991	43.3	1,366

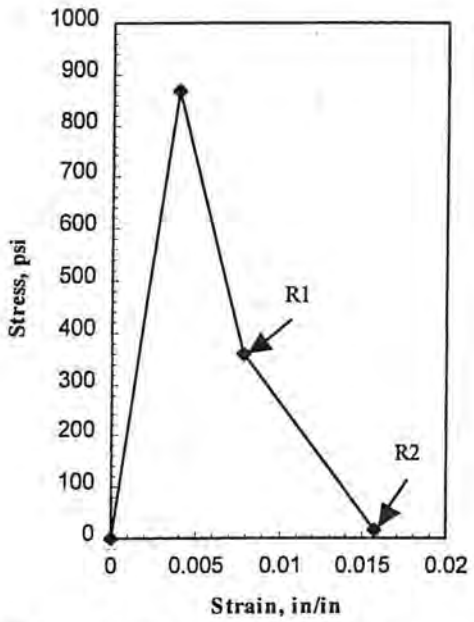

Figure 14 — Stress-strain curve for coal.

Description of the gob model. Although the material making up the gob is the same as the immediate roof strata, the environment is different and the gob material can be considered as a different material from the in-situ rock and acts differently. Generally speaking, the gob material is strain hardening, i.e., the modulus of deformation increases with increasing compaction.

Based on the Terzaghi's model describing the compaction behavior of granular material, a stress-strain relationship for the gob material was established (Pappas and Mark, 1993)

$$\sigma = \frac{E_i}{a}\left(e^{\varepsilon a} - 1\right) \qquad (4)$$

where
E_i is the initial modulus,
σ is the normal stress,
ε is the normal strain and
a is a constant.

The value of constant a is assumed to be (Zipf, 1992)

$$a = \frac{E_f - E_i}{n\sigma_v} \qquad (5)$$

where
E_f is the final modulus equals to the modulus of intact strata,
σ_v is the virgin vertical stress and
n is the gob height factor.

The gob height factor n is the ratio of the height of the caving zone to the thickness of coal seam and typically ranges from 2 to 8.

Based on Eqs. (4) and (5), Fig. 15 shows the stress-strain relationships for the gob materials in the upper and lower seams where the initial modulus and the gob height factor are 1,000 psi and 4.5, respectively. To implement the above gob model in finite element modeling, a special algorithm was incorporated in ABAQUS. This algorithm has been verified by in situ measurements (Morsy and Peng, in 2001).

Results and discussions

The main roof of the seam of interest contains a thick layer of fairly strong sandstone. Fully grouted 15.9-mm- (0.625-in.-) diam, 1.2-m- (4-ft-) long resin bolts in 1.2- x 1.2-m (4- x 4-ft) pattern with straps were used. All photos taken for that mine after failure (Figs. 9 and 10) show that there were no roof failures in this mine. Therefore, the analysis in this paper focuses on the stability of coal pillars. The two factors that could affect pillar stability were the interaction between the lower seam and the upper mined out seam and between the lower seam and the wet floor.

Effect of multiple-seam mining. The upper seam is mined out first, followed by the lower seam three to four months later. The amount of sandstone located within the interburden is a critical parameter in pillar load transfer. According to Haycocks and Karmis (1983), the relationship between the interactive distance and percentage of sandstone for room-and-pillar mines is given by

$$I = 110 - 0.42S \qquad (6)$$

where
I is the interactive distance, in feet, above which no interaction damage may be expected from room-and-pillar mining and
S is the percentage of sandstone in the interburden.

Using the typical stratigraphic column for the study area

(Fig. 7), the sandstone layer constitutes 70% of the 7.3-m- (155-ft-) thick interburden strata. Therefore, it can be concluded that without pillar extraction in the upper seam, no abutment pillar loading was expected from the upper seam to the lower seam.

Pillar mining was adopted in parts of the upper seam (Fig. 8). Hence, a high-stress zones might be encountered in the lower seam right below the gob-solid coal boundary of the upper seam. Figure 16 shows the position of the gob in the upper seam projected on the mine layout of the lower seam (i.e., seam of interest). The vertical stress contours in the gob of the upper seam, obtained from the global model, show that the virgin stress (204 psi or 1,400 kPa) was achieved at the central area of the gob. This means that a stress-transfer mechanism toward the gob had occurred in the upper seam. Therefore, this could reduce the intensity of stress transformation from the gob-solid coal boundary of the upper seam to the lower seam. Figure 17 shows the stress concentration distribution along Sections A-A and B-B (Fig. 16) in the lower seam at Stage No. 1. Along section A-A, the stress concentration effect of upper seam gob was observed at Pillars No. 3 and No. 9, while a stress relief was observed at Pillar No. 6. Along section B-B, the stress concentration effect of upper seam gob was observed at Pillars No. 2 and No. 9, while a stress relief was observed at Pillar No. 6.

Figure 18 shows the final configuration of gob (at Stage No. 3) in the lower seam before failure. It is obvious that the vertical stress (83 psi or 570 kPa) in the gob is very small compared to the virgin stress in this seam (377 psi or 2,600 kPa). This could be due to the beam effect of the thick sandstone layer in the main roof. Figure 19 shows the stress concentration distribution along sections A-A and B-B (Fig. 18) in the lower seam at Stage No. 3. It is obvious that there is a zone of high stress concentration around the gob of the lower seam.

Figure 20 shows the contours of stress concentrations for Pillars A, B, C and D during Stage No. 1. Compared to Pillars B, C and D, Pillar A has the highest average pillar stress concentration (2.148) and the lowest average pillar stability factor SF1 (1.433). The same behavior was observed during Stage No. 2. Hence, without considering the effect of weak floor conditions, the interaction between the upper and lower seam was observed, but it has no significant effect on the pillar stability of the lower seam.

Effect of weak floor conditions. Using the proposed numerical method for estimating the local mine stiffness, the local mine stiffness contours were obtained for different mining stages for Pillar B (Fig. 21). It is obvious that local mine stiffness (K_{LMS}) at any point of interest depends on its location within the pillar and the stage of mining.

Because the stress distribution in a pillar is not uniform, each pillar consists of points with different state of stresses, some in stable and others in unstable conditions. Figure 22 represents the typical condition for unstable parts of Pillar B. The unstable parts reached their peak strengths within the Stage No. 2 (Fig. 22 A). As a result of wet floor condition in Stage No. 3, the vertical stresses in these parts dropped sharply, while the strain increased slightly. Figure 22 B shows that

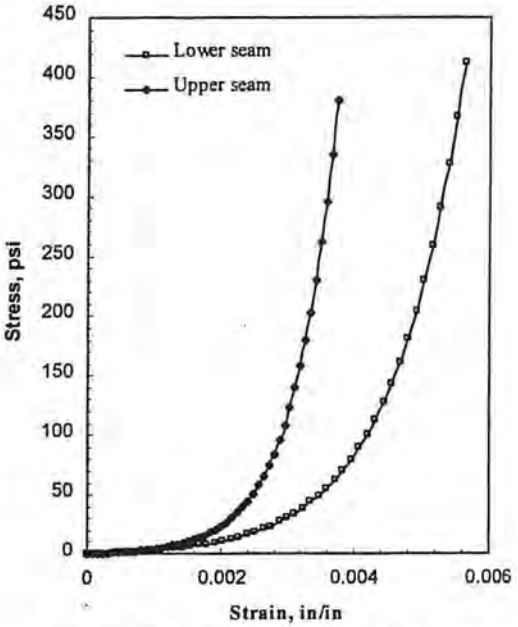

Figure 15 — Stress-strain curve for gob.

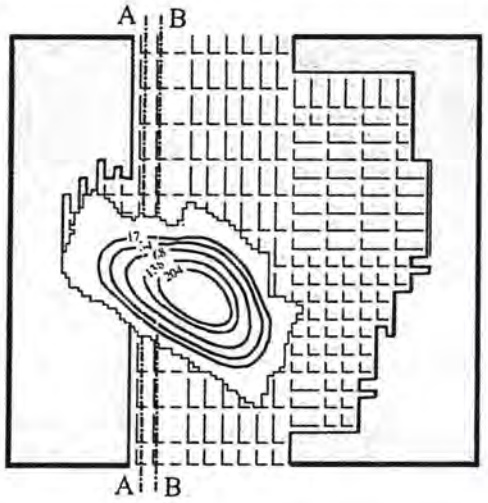

Figure 16 — Contours of vertical stress (psi) in the gob of the upper seam, projected on the lower seam.

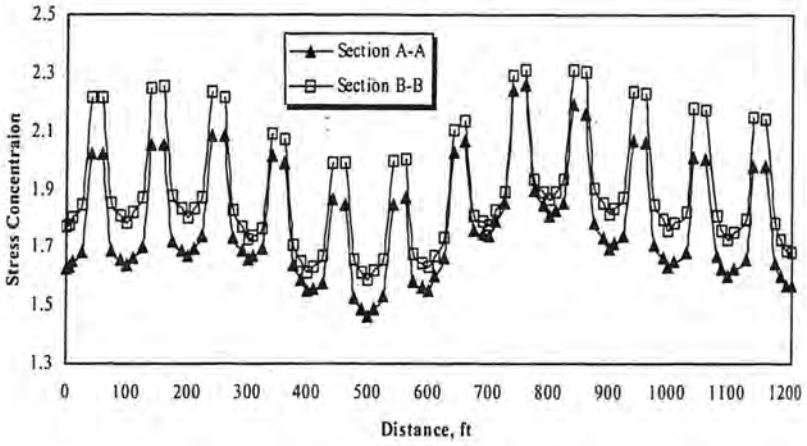

Figure 17 — Stress concentration along Sections A-A and B-B at Stage No. 1.

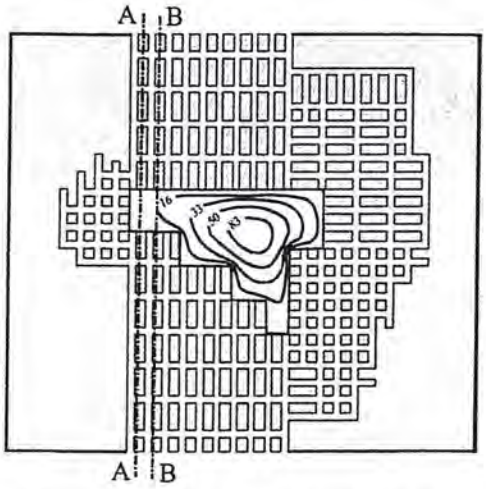

Figure 18 — Contours of vertical stress (psi) in the gob of the lower seam.

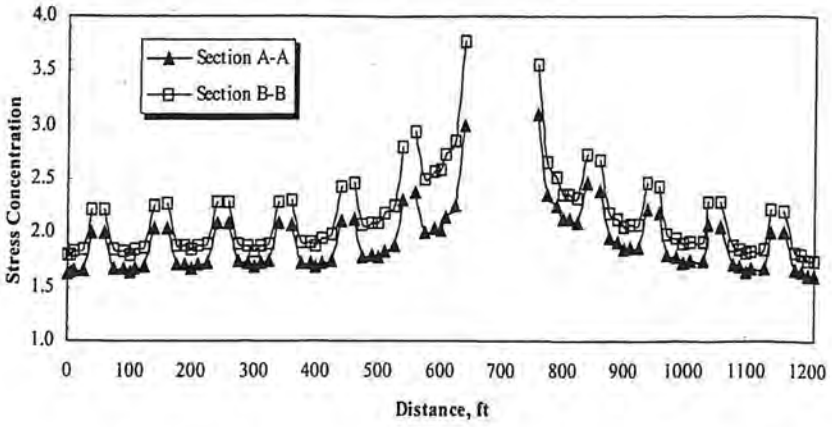

Figure 19 — Stress concentration along Sections A-A and B-B at Stage No. 3.

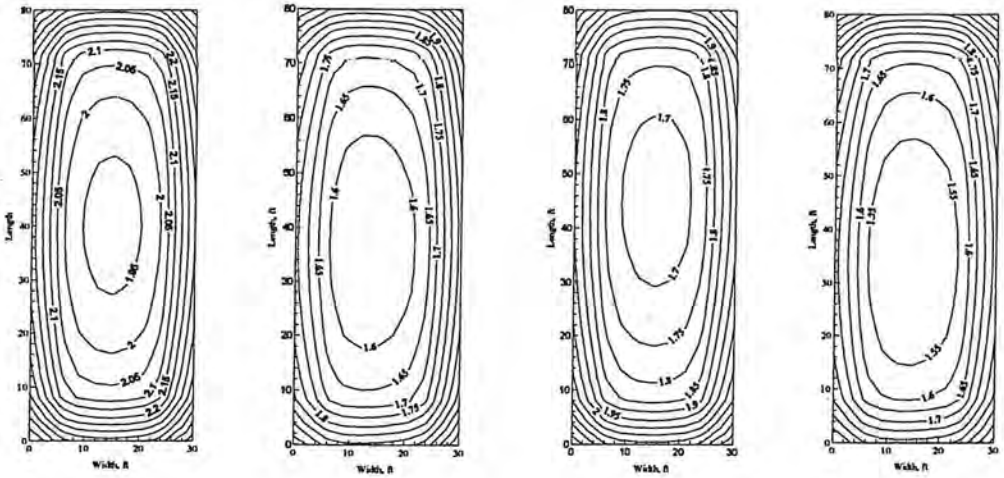

Pillar Location	A	B	C	D
Average (σ_{zz}/σ_o)	2.148	1.746	1.865	1.685
Average SF1	1.433	1.525	1.463	1.555

Figure 20 — Contours of tress concentrations (σ_{zz}/σ_o) at Stage No. 1 for Pillars A, B, C and D.

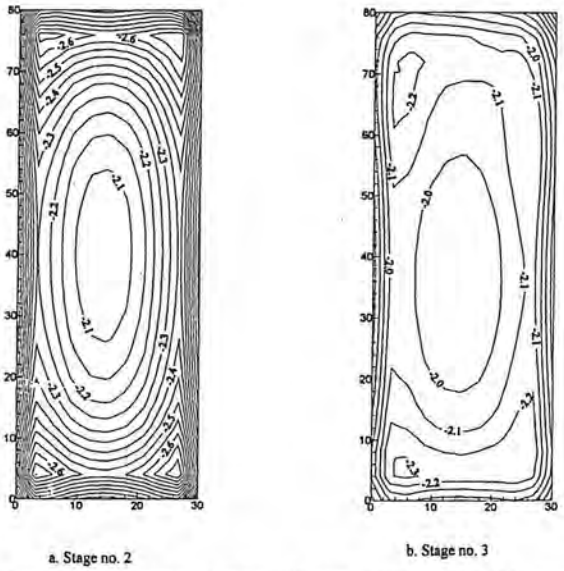

Figure 21 — Local mine stiffness contours (KLMS x 105 psi) for Pillar B at different mining stages.

the local mine stiffness (K_{LMS}) at Stage No. 3 was smaller than the postfailure slope (K_p) of the stress-strain curve.

Figure 23 is the typical representation for stable parts of Pillar B. The parts behave elastically up to Stage No. 2. During Stage No. 3, these parts start to yield, but the condition of stability was satisfied, i.e., that the local mine stiffness (K_{LMS}) was greater than the post-failure slope (K_p) of the stress-strain curve (Fig. 23 B).

Figure 24 summarizes the global stability factors SF1 and SF2 for Pillar B. According to the proposed stability criteria, Pillar B was stable during Stages No. 1 and No. 2 and became unstable when the immediate floor became weak in Stage No. 3.

Using the estimated local stability factor LSF2 for Pillar B, the unstable yielding zones were defined at Stage No. 3, for different pillar sections (Fig. 25). The dark areas represent the unstable zones. It is obvious that large areas of unstable zones located at pillar sections close to the floor. In addition, the unstable zones concentrated at the perimeter of the pillar especially near the gob side.

Pillar C behaves elastically during Stages No. 1 and No. 2.

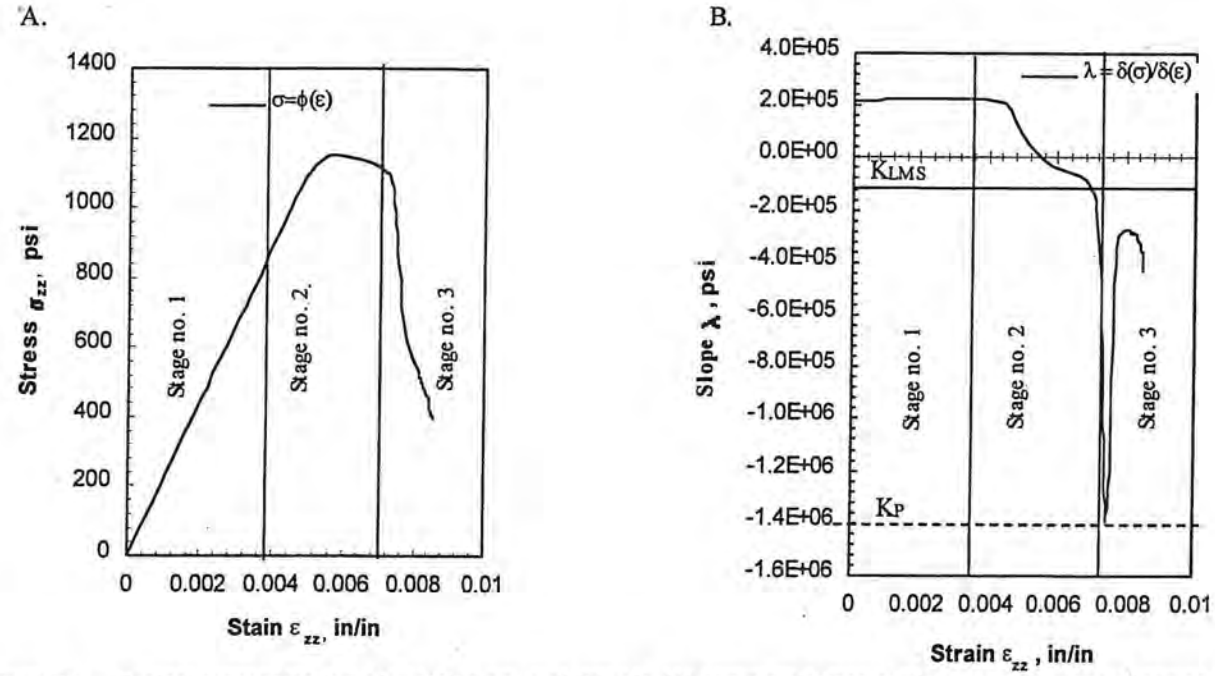

Figure 22 — Typical representation of unstable parts of Pillar B: (A) complete stress-strain curve; (B) slope of stress-strain curve vs. strain.

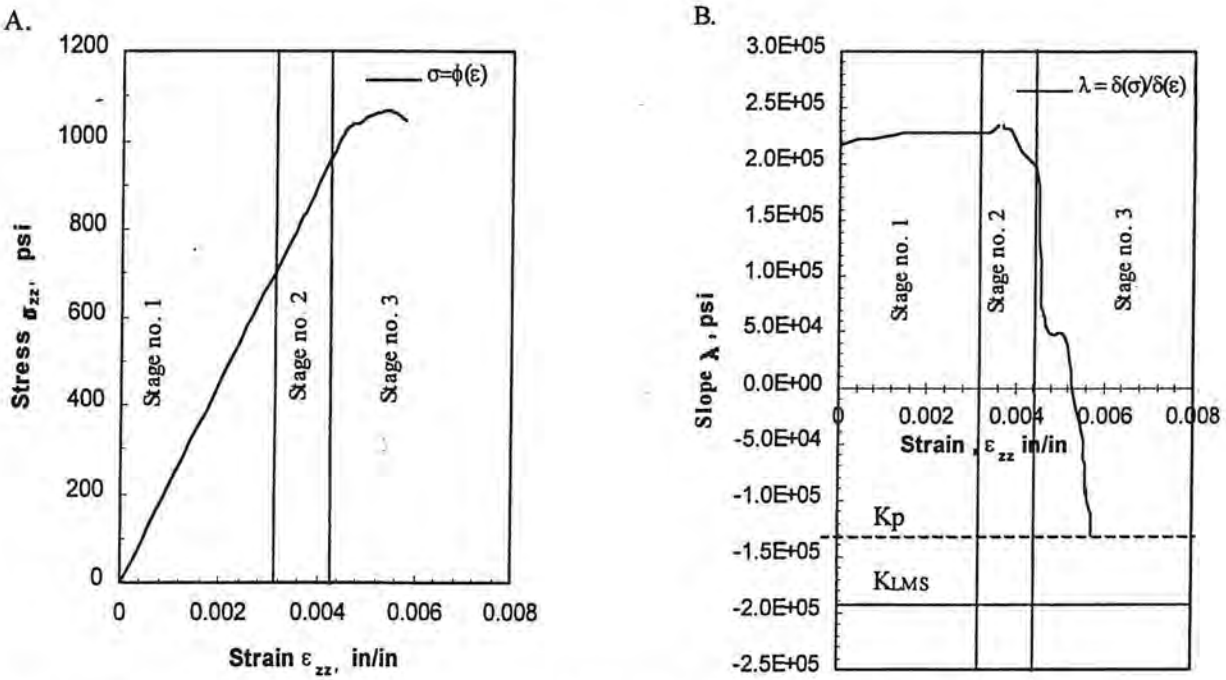

Figure 23 — Typical representation of stable parts of Pillar B: (A) complete stress-strain curve; (B) slope of stress-strain curve vs. strain.

By the end of Stage No. 3, every point within the pillar was very close to its yielding point. Figure 26 shows the global stability factors SF1 and SF2 for Pillar C at various stages. According to the proposed stability criteria, Pillar C was stable during Stages No. 1 and No. 2 and became critically stable in Stage No. 3. This means that any change in pillar geometry or reduction in pillar constraints provided by the roof and/or floor will turn it into unstable condition. As a result of mining parts of the pillar, a fourth mining stage was assumed for Pillar C. At Stage No. 4, a sudden drop in the slope of the stress-strain curve for every point within Pillar C was observed.

At Stage No. 4, most points in Pillar C became unstable because the local mine stiffness (K_{LMS}) at Stage No. 4 was smaller than the postfailure slope (K_p) of the stress-strain curve. Also, there were some stable points in Pillar C, even though their state of stress was in the postpeak region.

The calculated local stability factors LSF2 for Pillar C at Stages No. 3 and No. 4 show how the pillar became unstable during Stage No. 4. Figure 27 shows the image of LSF2 for a section of Pillar C, at an elevation of 1.12 m (3.67 ft) from the floor, during Stages No. 3 and No. 4. It is obvious that the unstable yielding zones (dark areas) covered most of the section in Stage No. 4. This behavior is confirmed by the

abrupt change in LSF2 when the pillar goes from Stage No. 3 to Stage No. 4, as shown in Fig. 26.

The condition in Pillar D is very similar to that in Pillar C. By the end of Stage No 3, most points in the pillar were very close to their yielding points. Figure 28 shows that the pillar was stable during Stages No. 1 and No. 2 but became critically stable at Stage No. 3. Therefore, it was expected that Pillar D could turn to unstable condition once the floor was deteriorated further, or additional unexpected loads were applied to the pillar. Because Pillar D was close to the Mains, it was further deduced that as water flows further outby, pillar deterioration would propagate further toward the Mains.

From the above analysis, the pillar stability can be evaluated by one of the following conditions:

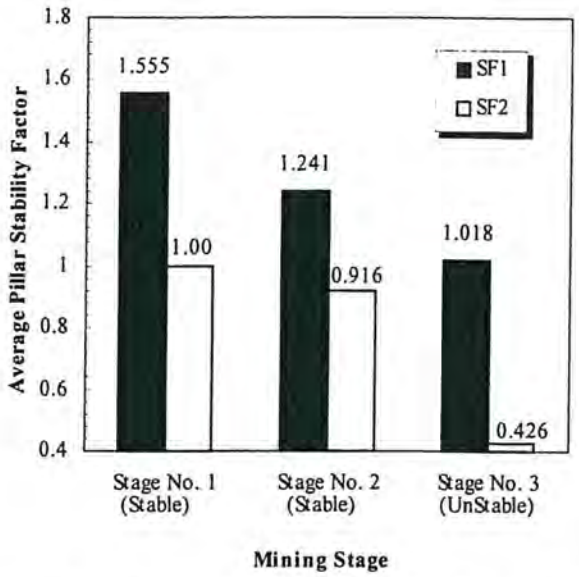

Figure 24 —Average pillar stability factors SF1 and SF2 for Pillar B at different mining stages.

- *Stable condition — SF1 > 1 and SF2 ≈ 1:* In this case, the majority of the state of stresses in the pillar lie in Region AB (Fig. 1) and the pillar behaves elastically.
- *Critically stable condition — SF1 ≈ 1 and SF2 > 0.5:* In this case, the majority of the state of stresses within the pillar lie in the Region BC (Fig. 1). Any change in pillar geometry or constraints provided by the surrounding strata could make the pillar unstable.
- *Unstable condition — SF1 ≈ 1 and SF2 ≤ 0.5:* In this case, more than 50% of the points in the pillar undergo unstable yielding and the pillar fails violently.

Summary of causes of massive pillar failure. According to this analysis and the available information, the massive pillar failure was initiated as a result of weak immediate floor conditions and the beam action of the main roof. The failure spreads to the Mains due to the critical stable condition of the coal pillars at the panel mouth and the further deterioration of immediate floor due to water pooling.

Conclusion

A new method of pillar stability evaluation was proposed and verified by a case of massive pillar failure. The proposed method has the following features:

- it considers the softening behavior of coal pillar;
- it contains a verified algorithm for gob simulation;
- it contains a new algorithm for local mine stiffness prediction;
- it predicts the stability of coal pillar in prepeak and postpeak regions; and
- it is able to predict several types of pillar stability, i.e., stable, unstable and critically stable.

In this study, the new algorithm for local mine stiffness prediction was presented and verified by analytical and numerical methods. The proposed algorithm is distinguished by its ability to predict the nonuniform distribution of local mine stiffness.

Using a case of massive pillar failure, the proposed pillar design was able to show:

- the changes of pillar stabilities at different stages of mining,
- that the failure can expand to the Mains and
- that the proposed stability factor SF2 is very sensitive to loading conditions of the pillar.

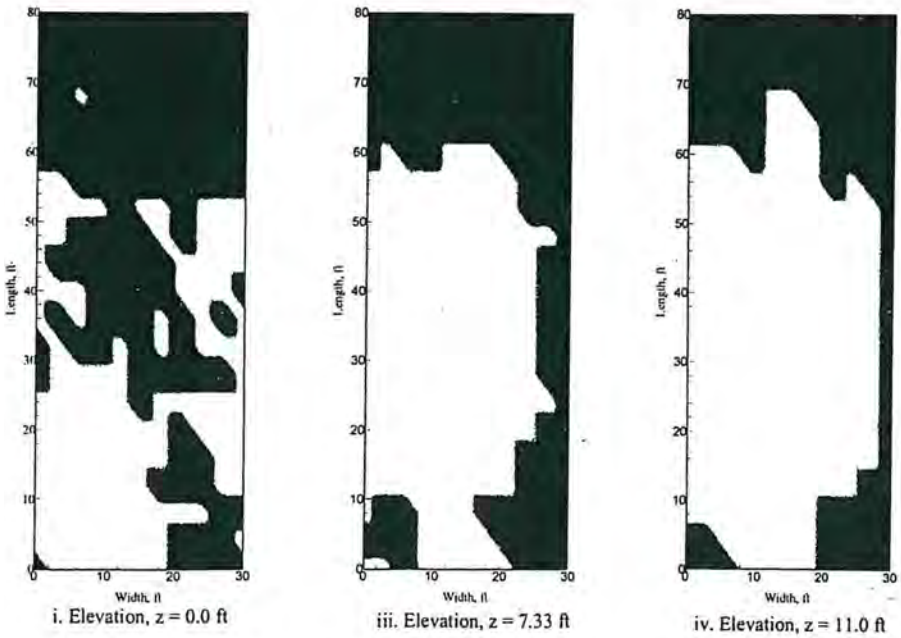

Figure 25 — Image of unstable yielding zones (dark areas) in Pillar B at Stage No. 3.

References

Chen, G., and Karmis, M., 1988, "Computer modeling of yield pillar behavior using post-failure criteria," *7th Int. Conf. Ground Control in Mining*, West Virginia University, pp. 116-125.

Chugh, Y., and Pytel, W., 1992, "Design of partial extraction coal mine layouts for weak floor strata conditions," *Proceedings of Workshop on Coal Pillar Mechanics and Design*, US Bureau of Mines, IC 9315, pp. 32-49.

Crouch, S.L., and Fairhurst, C., 1973, "The mechanics of coal mine bumps," US Bureau of Mines, Contract No. H0101778, February 22, 1973.

Das, M.N., 1986, "Influence of width/height ratio on postfailure of Coal," *Int. J. of Mining and Geological Eng.*, Vol. 4, pp. 79-87.

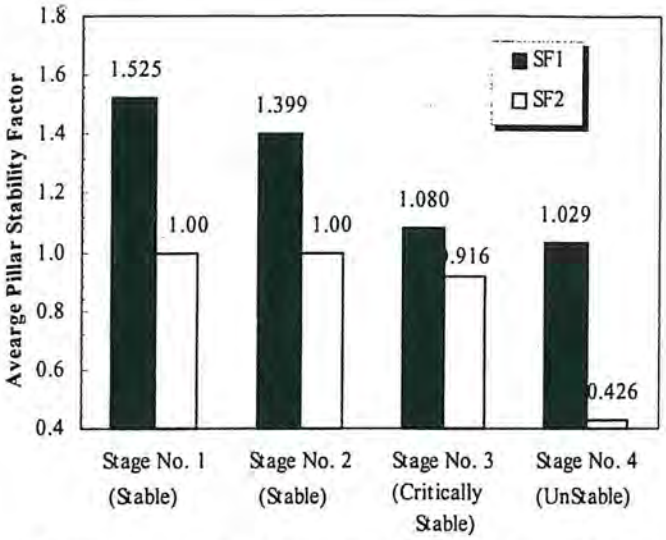

Figure 26 — Average pillar stability factors SF1 and SF2 for Pillar C at different mining stages.

Haycocks, C., and Karmis, M., 1983, "Ground control mechanisms in multi-seam mining, US Bureau of Mines OFR 7-84, 328 pp.

Hibbitt, D., Karlsoon, B., and Sorensen, P., 1998, "ABAQUS Manual," Version 5.7, Hibbitt, Karlsoon & Sorensen, Inc.

Karabin, G.J., and Evanto, M.A., 1999, "Experience with the boundary-element method of numerical modeling to resolve complex ground control problems," *Proc. of the 2nd Int. Workshop on Coal Pillar Mech. and Design*, NIOSH, IC 9448, pp. 89-113.

Morsy, K., and Peng, S., 2001, "Numerical modeling of gob loading mechanism in longwall coal mines," *21st Int. Conf. Ground Control in Mining*, West Virginia University, pp. 58-67.

Pappas, D.M., and Mark, C., 1993, "Behavior of simulated longwall gob material," US Bureau of Mines, RI 9458.

Pen, Y., and Barron, K., 1994, "The role of local mine stiffness in pillar bump prediction," *Proceedings of the 1st North American Rock Mechanics Symposium*, Austin, Texas, 13 June 1994, pp. 1017-1024.

Salamon, M.D.G., 1970, "Stability, instability and design of pillar workings," *Int. J. Rock Mech. Min. Sci.*, Vol. 7, pp. 613-631.

Sheorey, P.R , Barat, D., et al., 1995, "Application of yield pillar technique for successful depillaring under stiff strata," *Int. J. Rock Mech., Min. Sci. & Geomech. Abst.*, Vol. 32, No. 7, pp. 669-708.

Starfield, A.M., and Fairhurst, C., 1968, "How high-speed computers advance design of practical mine pillar systems," *Engineering & Mining Journal*, Vol. 169, Ed. 5, pp. 78-84.

Starfield, A.M., and Wawersik, W.R., 1968, "Pillars as structural components in room-and-pillar mine design," *Proc. of 10th U.S. Symp. on Rock Mech.*, Rice Univ., AIME, New York, pp. 793-809.

Su, D., and Hasenfus, G., 1998, "Effects of in-seam and bear-seam conditions on coal pillar strength," *17th Int. Conf. Ground Control in Mining*, West Virginia University.

Van Heerden, W.L., 1975, "In situ complete stress-strain characteristics of large coal specimens," *J. S. Aft. Inst. Min. Metall.*, March, pp. 207-217.

Wagner, H., 1974, "Determination of the complete load-deformation characteristics of coal pillars," *Proceedings of 3rd Int. Cong. on Rock Mechanics*, ISRM, Denver, Vol. 213, pp. 1076-1082

Zipf, K., 1992, "MULSIMNL theoretical and programmer's manual," US Bureau of Mines, IC 9321.

Zipf, K., 1999, "Using a post-failure stability criterion in pillar design," *Proc. of 2nd Int. Workshop on Coal Pillar Mechanics and Design*, NIOSH, IC 9448, pp. 181-192.

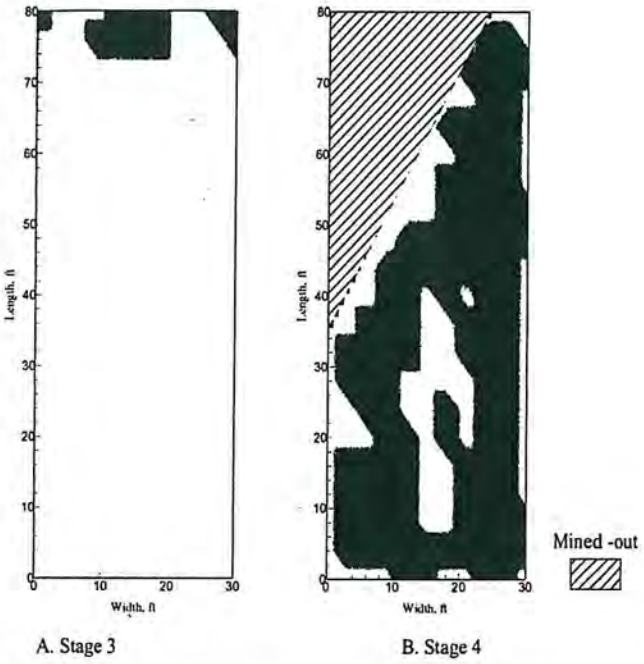

Figure 27 — Image of unstable zones (black areas) in Pillar C at Stages No. 3 and No. 4.

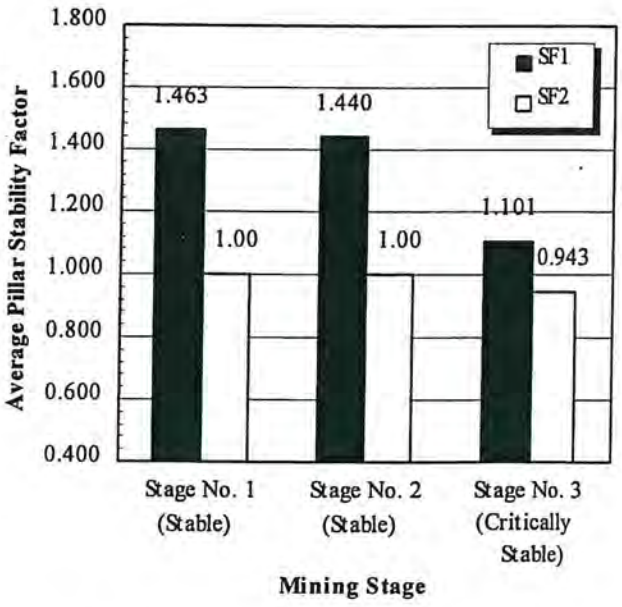

Figure 28 — Average pillar stability factors SF1 and SF2 at Location D for different mining stages.